GeoScienceWorld
Lithosphere
Volume 2022, Article ID 9211516, 15 pages
https://doi.org/10.2113/2022/9211516

Lithosphere

Research Article

Mechanical Properties and Failure Behavior of Mortar-Encased Coal Bodies under Impact Loads: Insights from Experimental Investigation

Kai Wang[1,2], **Jinwen Bai**[1,2,3], **Guorui Feng**[1,2], **Dawei Yin**[3], **Boqiang Cui**[1,2], **Xudong Shi**[1,2] and **Xinyu Yang**[1,2]

[1]*College of Mining Engineering, Taiyuan University of Technology, Taiyuan 030024, China*
[2]*Key Laboratory of Shanxi Province for Mine Rock Strata Control and Disaster Prevention, Taiyuan 030024, China*
[3]*State Key Laboratory of Mine Disaster Prevention and Control, Shandong University of Science and Technology, Qingdao 266590, China*

Correspondence should be addressed to Jinwen Bai; baijinwen629@sina.com and Guorui Feng; fguorui@163.com

Received 2 June 2022; Accepted 16 July 2022; Published 24 August 2022

Academic Editor: Shaofeng Wang

Failure of residual coal pillars under dynamic load disturbances can induce goaf collapse, ground subsidence, or coalbursts. Encasing the residual coal pillar in mortar is an effective method for reinforcing the residual coal pillar. However, the mechanical behaviors of mortar-encased coal bodies under impact loads remain poorly investigated. In this study, impact tests were conducted on coal, mortar, and mortar-encased coal specimens using a split Hopkinson pressure bar (SHPB) system. The mechanical properties and failure behavior of the mortar-encased coal specimens under impact loading were systematically investigated in terms of several metrics including dynamic stress-strain curves, failure patterns, strength change characteristics, and energy consumption laws. Results show that, owing to the different mechanical properties of the coal and mortar elements in the composite specimens, the mortar-encased specimen has a nonlinear deformation characteristic. The mortar has a higher energy absorption rate compared to the coal. Additionally, increasing the thickness of the external mortar body is helpful for absorbing more stress wave energy and increasing the dynamic strength of the mortar-encased coal specimens. Furthermore, under low strain rate loading, the external mortar body of the composite specimen initially experienced axial splitting failure. With increasing strain rate, axial splitting failure occurred in both the external mortar body and inner coal body. This study provides useful guidelines for reinforcing residual coal pillars in underground engineering.

1. Introduction

In underground coal mining, coal pillars of different sizes are extensively designed as the support structure of the mining space [1, 2]. Once coal resources in the working face are fully mined out, coal pillars are permanently abandoned in the mine [3, 4]. The Datong mining areas in China encompass a large number of residual coal pillars [5, 6]. These residual coal pillars are not only subjected to an overburdened load for a long time but are also affected by mining disturbances and water erosion [7, 8]. Under the coupling effect of these factors, residual coal pillars are prone to damage and instability. The instantaneous instability of residual coal pillars can lead to a chain of adjacent pillar instabilities in the goaf [9, 10]. In severe cases, it may cause goaf collapse, surface subsidence, and coalbursts [11–13].

Strengthening residual coal pillars is essential for ensuring green mining of coal mines [14, 15]. The most common reinforcement methods are shotcreting or infilling with solid materials in addition to coal pillars [16, 17]. After the coal pillar is wrapped with mortar, a composite bearing structure is formed to jointly bear the overburden load and resist the external disturbance load [18]. Therefore, an accurate assessment of the mechanical properties and failure mechanism of a composite bearing structure is critical for maintaining the stability of the overlying strata. The original residual coal

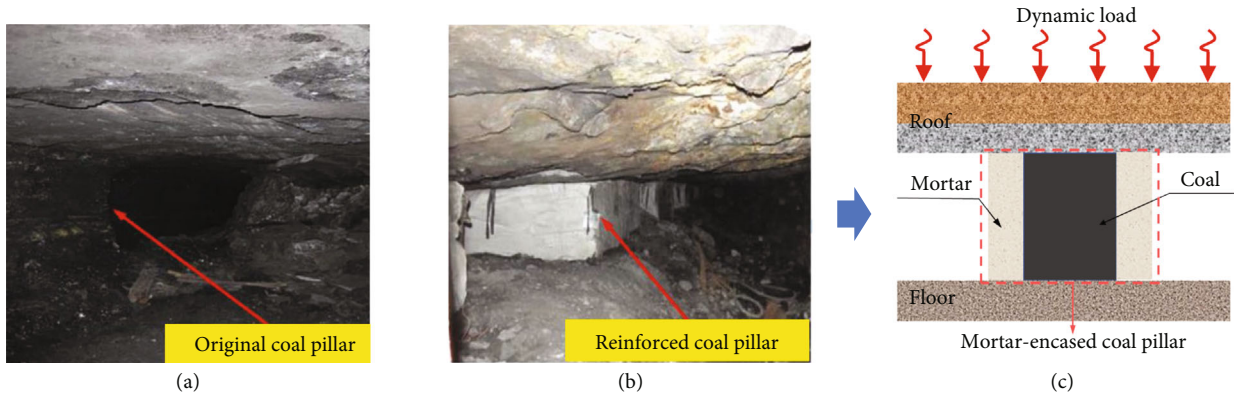

FIGURE 1: Photos of actual mortar-encased coal pillars: (a) original coal pillar [17], (b) reinforced coal pillar [17], and (c) stress diagram of reinforced coal pillar.

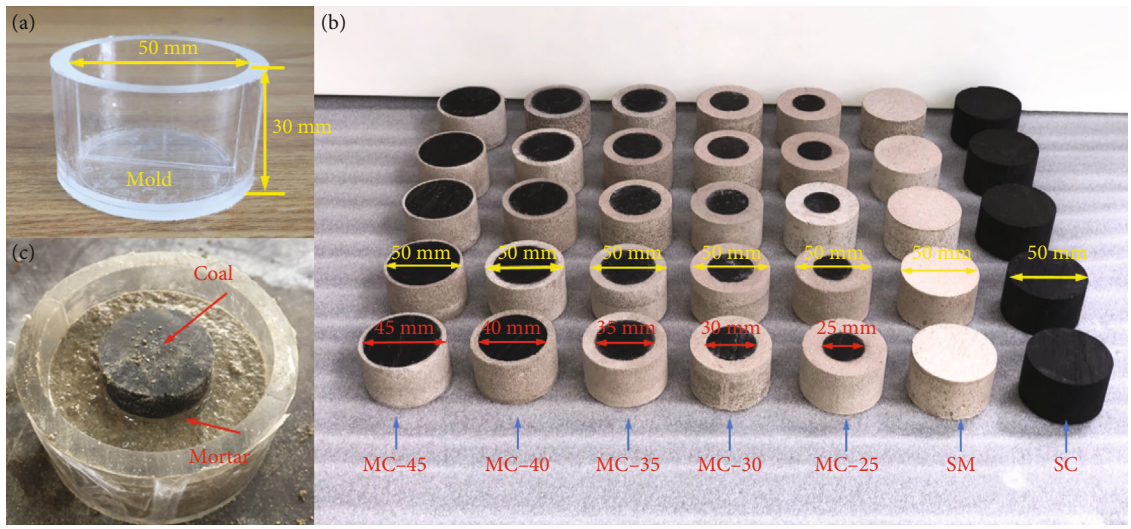

FIGURE 2: Preparation process of the study specimens: (a) mold physical map, (b) specimen after demolding, and (c) specimen pouring process.

pillar and encased coal pillars in an actual construction process are shown in Figure 1 [17].

Extensive research has been conducted on the stability of coal (mine) pillars including in situ tests [19–21], laboratory tests [22–25], numerical simulations [26–28], and theoretical calculations [29–31]. Laboratory experiments are the most common form of research performed in this direction. Yao et al. [32] investigated the mechanical behavior of coal samples under uniaxial compression and revealed their crack propagation characteristics. Gao and Kang [33] found that increasing the confining pressure could increase the residual strength of coal pillars. Peng et al. [34] proposed a damage evolution model for coal under triaxial confining pressure. Zhou et al. [35] used a coal pillar-roof physical model to investigate the stress evolution path of the mining space when the coal pillar group failed. Zhang et al. [17] found that encased coal pillars exhibit double-peaked stress-strain behavior under uniaxial compression. The above works provide useful guidance for the reinforcement protection of coal pillars under static loads.

However, with high-intensity mining activities in China, dynamic disasters frequently occur [36–39]. Reinforced residual coal pillars are not only subjected to static loads but are also inevitably affected by disturbance-induced dynamic loads, such as the dynamic loads triggered by hard roof breaking, fault activation, or rock blasting [40, 41]. Thus, it is necessary to evaluate the influence of the impact load on the reinforcement of residual coal pillars. Meanwhile, more information about the dynamic behavior of composite bearing structures under dynamic disturbances should be obtained.

Existing research shows that the strain rate of a dynamic load caused by blasting, rock bursts, or hard roof breaking ranges from $10^1\ s^{-1}$ to $10^3\ s^{-1}$ [42–45]. According to previous research [46, 47], the SHPB system can be used to study the dynamic mechanical behavior of rock materials in this range. Therefore, impact tests were conducted on mortar, coal, and mortar-encased coal specimens with different radius ratios. The dynamic stress-strain curves, failure patterns, strength change characteristics, and energy conversion

Table 1: Test results of the coal and mortar under quasistatic conditions (loading velocity is 0.002 mm/s).

Specimen	Uniaxial compression strength (MPa)	Elastic modulus (GPa)	Compressional wave velocity (m/s)	Poisson's ratio	Density (kg/m^3)
Coal	19.67	2.33	1985	0.40	1358
Mortar	20.39	4.65	1350	0.15	1286

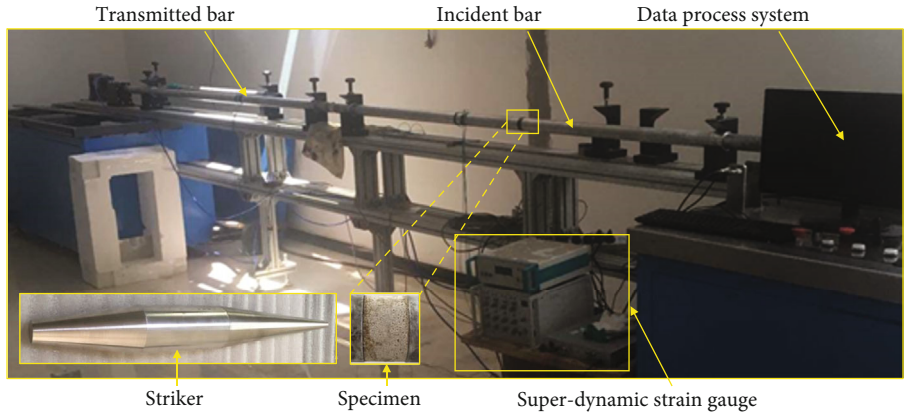

Figure 3: SHPB test system.

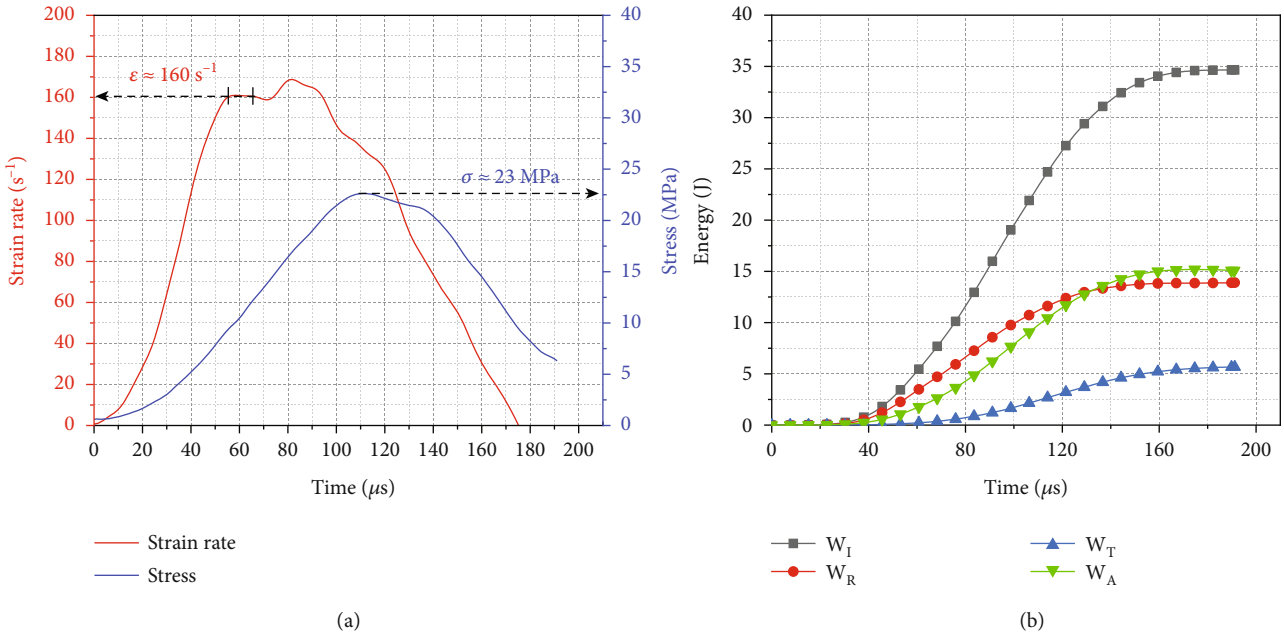

Figure 4: Processing results of test data: (a) the stress and strain rate and (b) the incident, reflection, transmission, and absorption energy.

laws of the three specimen types were comprehensively analyzed.

2. Materials and Methods

2.1. Specimen Preparation. The test specimens included a single coal (SC), single mortar (SM), and mortar-encased coal (MC). All specimens were made into cylinders ($\phi 50 \times 30$ mm) to meet the standards of rock dynamics tests [43, 44]. The two loading surfaces of each specimen were carefully ground to eliminate the effect of interfacial friction.

Coal specimens were prepared from fresh coal blocks by means of drilling, cutting, and grinding. Mortar specimens were made of water, P. O 42.5 cement, and river sand, with a corresponding ratio of 0.7 : 1 : 1.3 [17]. The preparation process was as follows. First, a small amount of lubricating

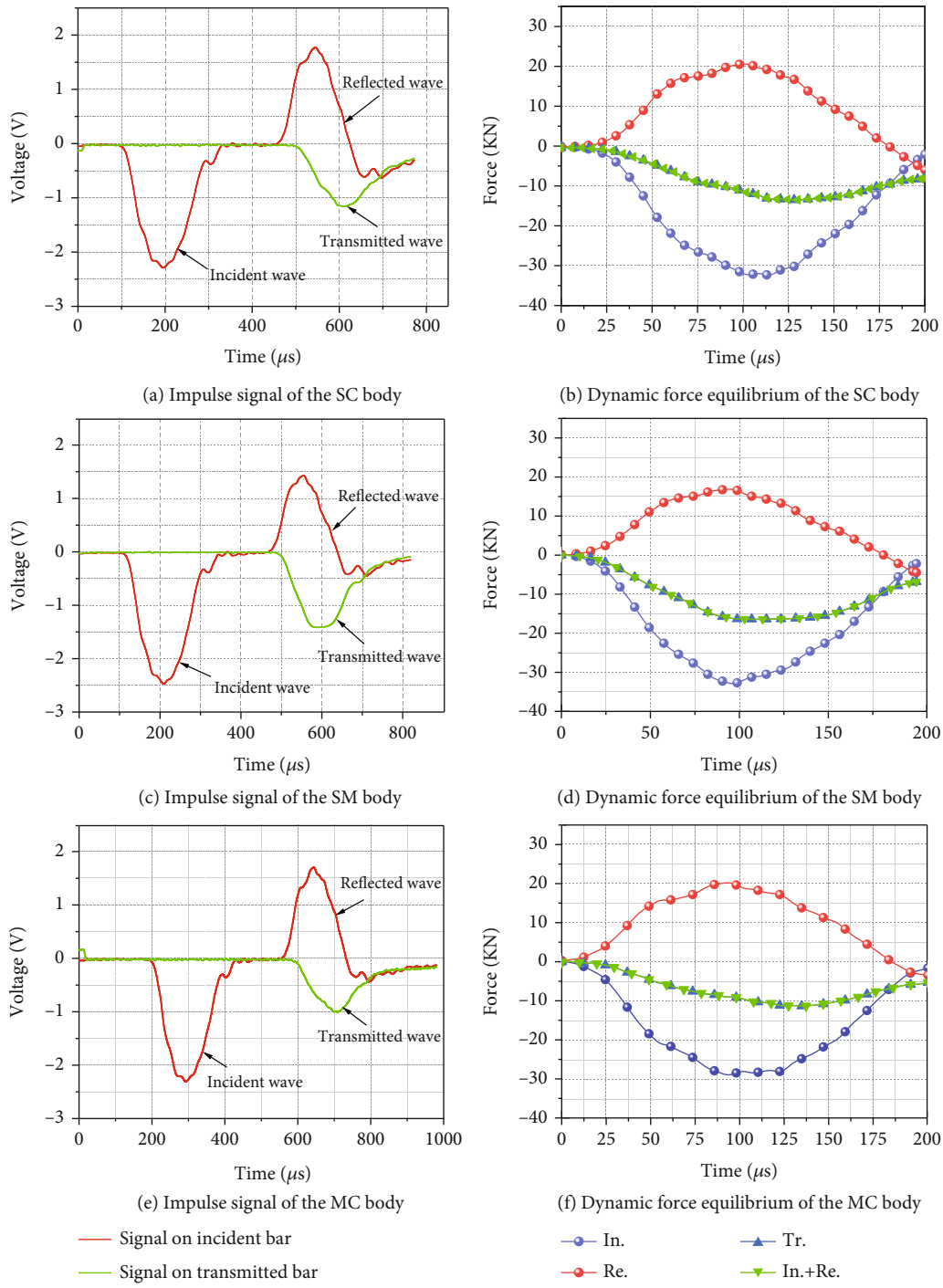

Figure 5: Dynamic stress equilibrium verification of typical specimens.

oil was applied to the mold (Figure 2(a)) to facilitate specimen demolding. Second, the cement, sand, and water were thoroughly mixed according to the specified mass ratio. After 24 h, the mixture was demolded and placed into a maintenance box for 28 days. The mechanical parameters of the coal and mortar under static loads are listed in Table 1.

Each mortar-encased coal specimen was a combination of the coal and mortar elements. The mortar-encased coal specimens had five different mortars. Coal-radius ratios and the corresponding thicknesses of the encasing mortar were 2.5, 5, 7.5, 10, and 12.5 mm, as shown in Figure 2(b). Taking MC-25 as an example, the preparation process was as follows: first, a cylindrical coal specimen ($\phi 25 \times 30$ mm) was prepared from the coal blocks. The coal specimen was then placed at the center of the mold. Second, the fully mixed mortar was poured into a mold, as shown in Figure 2(c). Finally, after 24 h, the mixture was demolded and cured for 28 days.

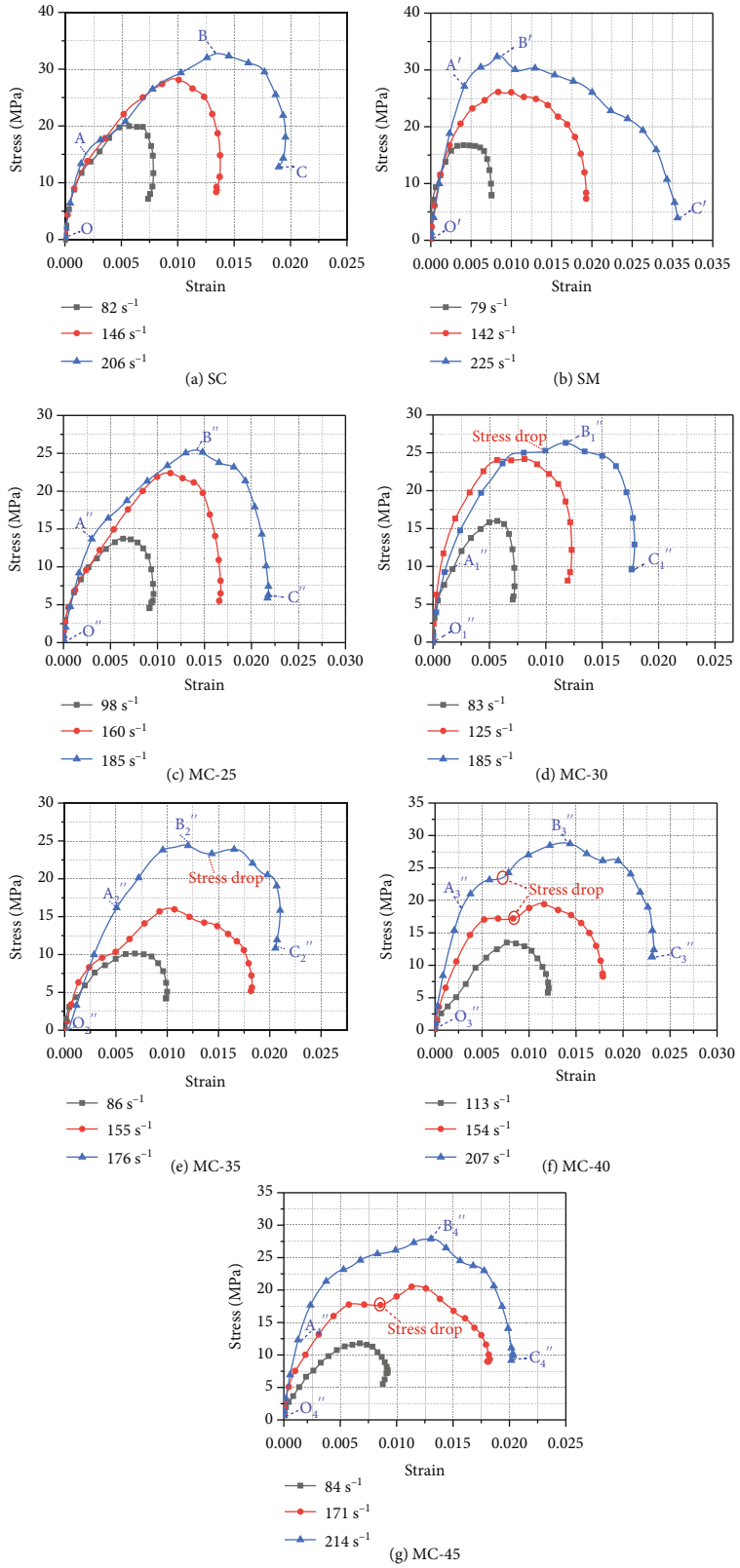

Figure 6: Dynamic stress-strain curves.

2.2. Testing Apparatus and Methodology. In this study, the impact test system mainly included an air compressor, two pressure bars ($\phi 50 \times 2500$ mm), striker bar, superdynamic strain instrument, strain acquisition card, and data processing system, as shown in Figure 3. The incident, transmitted, and striker bars were made of 7075 aluminum alloy. The

striker bar used in this study was cone-shaped, which is beneficial for realizing constant strain rate loading of the specimen [48, 49].

Four different impact pressures (0.1, 0.15, 0.2, and 0.25 MPa) were used to load the specimens. After completing the impact testing, we selected sieves with apertures of 40, 30, 25, 20, 10, 5, 2, 1, 0.5, 0.25, and 0.075 mm to sieve the broken specimens and analyze the fragmentation characteristics.

2.3. Data Processing. During the test, two stress pulse signals were produced in the pressure bars: incident and reflected waves [50]. All stress pulses were captured by a superdynamic strain gauge. Following the SHPB theory [51, 52], the strain rate ($\dot{\varepsilon}(t)$), strain ($\varepsilon(t)$), and stress ($\sigma(t)$) of a specimen can be further processed using

$$\begin{aligned}\dot{\varepsilon}(t) &= \frac{C_b}{L}[\varepsilon_i(t) - \varepsilon_r(t) - \varepsilon_t(t)],\\ \varepsilon(t) &= \frac{C_b}{L}\int_0^t [\varepsilon_i(t) - \varepsilon_r(t) - \varepsilon_t(t)]dt,\\ \sigma(t) &= \frac{A_b}{2A}E_b[\varepsilon_i(t) + \varepsilon_r(t) + \varepsilon_t(t)],\end{aligned} \tag{1}$$

where $\varepsilon_i(t)$, $\varepsilon_r(t)$, and $\varepsilon_t(t)$ correspond to the incident, reflected, and transmitted strains of the pressure bar, respectively, and A_b, E_b, and C_b are the cross-sectional area, elastic modulus, and P wave velocity of the pressure bars, respectively. t is the time for the stress pulse to propagate in the specimen, L and A are the length and cross section of the specimen, respectively. Typical dynamic stress and strain rate calculation curves for the specimen (No. MC-25-1) are shown in Figure 4(a).

In addition, the incident, reflected, and transmitted energies of the sample during the impact are represented by W_I, W_R, and W_T. These three energies can be obtained using [53–55]

$$\begin{aligned}W_I &= A_b C_b E_b \int_0^t \varepsilon_i^2(t)dt,\\ W_R &= A_b C_b E_b \int_0^t \varepsilon_r^2(t)dt,\\ W_T &= A_b C_b E_b \int_0^t \varepsilon_t^2(t)dt.\end{aligned} \tag{2}$$

Following the energy conservation law [46], the absorbed energy of the specimen (W_A) during the loading process can be deduced from Equation (3). Figure 4(b) presents four energy evolution curves for a typical specimen (MC-25-1).

$$W_A = W_I - W_R - W_T. \tag{3}$$

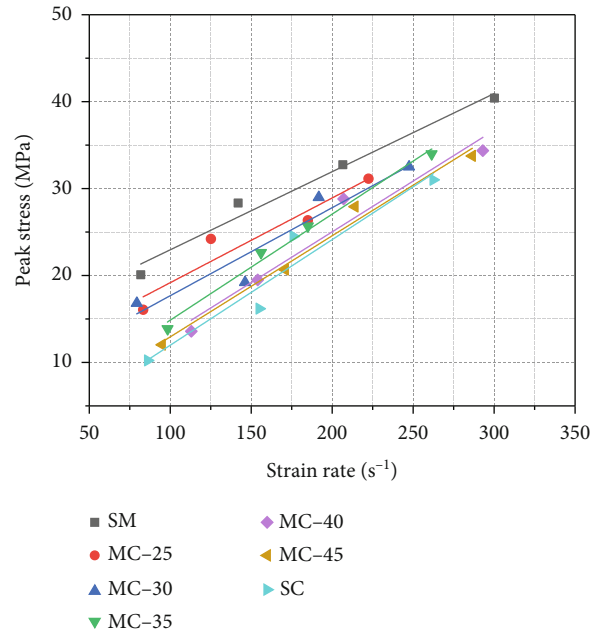

Figure 7: Variation of dynamic compressive strength with different strain rates.

To evaluate the energy evolution of the specimens, the ratio of W_A to W_I is usually defined as the energy utilization rate K_w [56, 57]:

$$K_w = \frac{W_A}{W_I} \times 100\%. \tag{4}$$

Previous studies [51, 54] have proven that the impact energy absorbed by the specimen during the failure process is mainly consumed in three forms: thermal, fracture, and kinetic energy. The kinetic and thermal energies were negligible. Hence, the dissipated energy (W_D) in the coal specimens was approximately equal to the absorbed energy (W_A). Moreover, the ratio of absorbed energy (W_A) to the volume of the test specimen (V) is usually defined as the energy dissipation density (η_w) of a specimen, which can be calculated using [58–60]

$$\eta_w = \frac{W_A}{V} \times 100\%. \tag{5}$$

After the impact test, all the failed specimens were screened with different sieve sizes. To quantify the degree of fragmentation of the specimen under different impact loads, formula (6) [56, 61] was used to calculate the average fragmentation (r_m) of the specimen.

$$r_m = \frac{\sum w_i \bar{r}_i}{\sum w_i}, \tag{6}$$

where $\bar{r}_i$ is the average size of the broken pieces of two adjacent sieves and w_i is the mass percentage of the broken pieces obtained from the two adjacent sieves.

Table 2: Summary of SHPB test results of specimens.

Numbers	Strain rate (s^{-1})	Incident energy (J)	Reflected energy (J)	Transmitted energy (J)	Absorbed energy (J)	Absorbed energy per unit volume (J/cm^3)	Energy utilization efficiency (%)
SC-1	82	14.64	3.63	4.86	6.15	0.08	42.01
SC-2	146	37.95	13.32	8.68	15.95	0.27	42.04
SC-3	206	60.84	13.56	20.14	27.14	0.46	44.61
SC-4	300	112.76	49.38	11.96	51.42	0.88	45.60
SM-1	79	12.89	2.86	4.02	6.01	0.10	46.63
SM-2	142	31.80	11.86	4.88	15.06	0.26	47.36
SM-3	166	58.92	19.49	10.90	28.53	0.48	48.43
SM-4	248	95.09	37.31	11.84	45.94	0.78	48.33
MC-25-1	98	13.16	4.88	2.54	5.74	0.10	43.62
MC-25-2	160	35.88	14.29	5.70	15.89	0.27	44.30
MC-25-3	185	56.04	23.04	7.30	25.70	0.44	45.86
MC-25-4	261	104.96	43.84	12.11	49.01	0.74	46.69
MC-30-1	83	12.15	3.23	3.58	5.34	0.10	43.92
MC-30-2	125	33.02	8.59	9.85	14.58	0.27	44.15
MC-30-3	185	52.58	18.64	10.44	23.50	0.42	44.69
MC-30-4	222	84.88	34.26	11.69	38.93	0.66	45.86
MC-35-1	86	10.62	4.65	1.44	4.53	0.08	42.66
MC-35-2	155	30.85	14.31	2.99	13.55	0.22	43.92
MC-35-3	176	51.55	19.77	8.44	23.34	0.40	45.28
MC-35-4	262	94.59	39.71	11.29	43.59	0.74	46.08
MC-40-1	113	15.66	6.93	2.00	6.73	0.11	42.97
MC-40-2	154	35.68	15.36	5.54	14.78	0.27	41.43
MC-40-3	207	68.48	26.21	12.44	29.83	0.53	43.56
MC-40-4	293	108.02	42.08	18.59	47.35	0.67	43.83
MC-45-1	95	15.45	6.83	2.00	6.62	0.11	42.88
MC-45-2	171	42.60	19.48	4.82	18.30	0.31	42.96
MC-45-3	214	63.37	26.07	9.68	27.62	0.50	43.59
MC-45-4	286	110.61	48.94	10.90	50.77	0.86	45.90

3. Experimental Results

3.1. Dynamic Force Equilibrium. To ensure the validity of the test results, it was necessary to verify the dynamic force equilibrium of each specimen [62, 63]. In this study, the dynamic force equilibrium of all the specimens was checked. Figure 5 shows the original stress wave signals of the coal (No. SC-1), mortar (No. SM-1), and mortar-encased specimens (No. MC-25-1) during the impact process and dynamic force balance verification curves. It can be concluded that a similar half-sine stress wave was produced in the pressure bar, and the time taken by the stress wave to propagate in the specimen was approximately 200 μs. In addition, the superposition curve of the incident and reflected stresses coincides with the transmission stress curve, which indicates that the test results are credible.

3.2. Dynamic Stress-Strain Characteristics. The representative dynamic stress-strain curves of the coal, mortar, and mortar-encased specimens are shown in Figure 6. Comparison of Figures 6(a) and 6(b) reveals that single coal specimens and single mortar specimens mainly include three deformation stages: (1) elastic deformation stage OA ($O'A'$): the strain of the specimen increased linearly with stress; (2) rapid crack growth stage AB ($A'B'$): the internal cracks in the specimen continued to initiate and expand rapidly during the propagation of the stress wave; and (3) postpeak fracture stage BC ($B'C'$): at this stage, a macrofracture surface is formed in the specimen. However, there are some differences between coal and mortar. The unstable crack propagation stage (AB) of coal is longer than that of mortar ($A'B'$), while a postpeak fracture stage (BC) of coal is significantly shorter than that of mortar ($B'C'$). This indicates that coal has more brittle failure characteristics than mortar.

The dynamic stress-strain curves of the mortar-encased specimens are shown in Figures 6(c)–6(g). It can be concluded that the mortar-encased specimens under different impact loads also included three deformation stages (elastic deformation stage, rapid crack growth stage, and postpeak

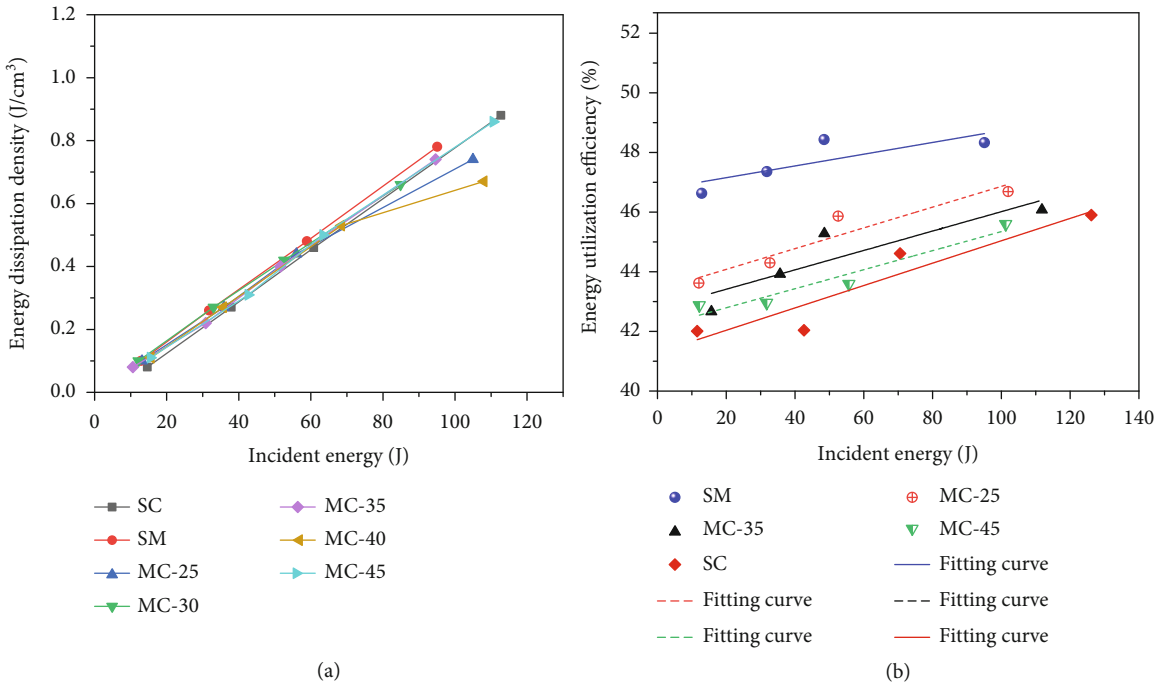

Figure 8: Energy dissipation characteristics of different specimens: (a) energy dissipation density and (b) energy utilization efficiency.

fracture stage), but the deformation characteristics of each stage were slightly different from those of the single coal or mortar specimen. The proportion of the postpeak fracture stage ($B'' C''$) in the whole deformation process ($O'' C''$) of the composite specimens was larger than that of the single coal specimens, whereas it was smaller than that of the single mortar specimens. This phenomenon reveals that the failure process of the composite specimen gradually changed from brittle fracture to ductile deformation owing to the existence of the external mortar, which reduced the instantaneous fracture degree of the composite specimen. In addition, at medium and high strain rates, the nonlinear change characteristics of the mortar-encased specimen during the stress rise stage are more obvious, and a "stress drop" phenomenon is observed, as shown in Figures 6(d)–6(g). This difference is because mortar and coal are two types of solid materials with different wave impedances, and the stress-wave propagation efficiencies in the two media are different, which eventually leads to different degrees of damage to the external mortar body and internal coal body.

3.3. Dynamic Strength Characteristics. The relationship between the dynamic compressive strength and strain rate of the coal, mortar, and mortar-encased specimens is shown in Figure 7. The results show that the dynamic compressive strength of these three types of specimens increased linearly with increasing strain rate. Furthermore, the dynamic strength of the mortar specimens is significantly higher than that of the coal specimens. The dynamic strength of a mortar-encased specimen is larger than that of a coal specimen but smaller than that of a mortar specimen. Moreover, as the thickness of the external mortar increased, the strength of the mortar-encased specimens gradually increased. This indicates that increasing the thickness of the external mortar body can improve the deformation ability of the composite bearing structure under impact loads.

3.4. Energy Dissipation Characteristics. Rock materials undergo irreversible energy conversion before failure [64]. Obtaining the energy dissipation characteristics is helpful for macroscopically explaining the failure mechanism of the specimen. The energy consumption density and energy utilization efficiency of the coal, mortar, and mortar-encased specimens under different incident energy loading conditions were obtained based on Equations (4) and (5), and a summary of the SHPB test results is presented in Table 2. The variation in the energy dissipation characteristics of the specimens with the incident energy is shown in Figure 8. The energy consumption density of the coal, mortar, and mortar-encased specimens increased linearly with increasing incident energy, as shown in Figure 8(a). This reveals that with higher input energy of the disturbance load, more energy is absorbed per unit volume by the specimen and the coal pillar is more prone to instability. Furthermore, Figure 8(b) shows that the energy utilization efficiency of the coal, mortar, and mortar-encased specimens with different thicknesses increased linearly with increasing incident energy. For a given incident energy, the energy absorption efficiency of the mortar specimens was the highest, followed by that of the mortar-encased specimens, and the energy absorption efficiency of the coal specimens was the lowest. For mortar-encased specimens, such as MC-25, MC-35, and MC-45, under the same incident energy conditions, the energy absorption rate increased with increasing thickness of the external mortar body. These results indicate that the mortar body has a better energy absorption effect than

Figure 9: Failure modes of specimens under different impact loads.

the coal body, and the larger the proportion of mortar in the mortar-encased specimen, the more stress wave energy the specimen can absorb.

3.5. Progressive Failure Behavior and Fragmentation Analysis. The crack evolution observed from the impact testing contained potential information related to the composite body failure. Figure 9 shows the failure modes and crack propagation of the coal, mortar, and mortar-encased specimens under different strain rates. As shown in Figures 9(a) and 9(b), as the strain rate increased, the damage degree of the coal and mortar specimens continued to increase, gradually changing from an unbroken state to blocks, particles, or even powders. Meanwhile, comparing the failure

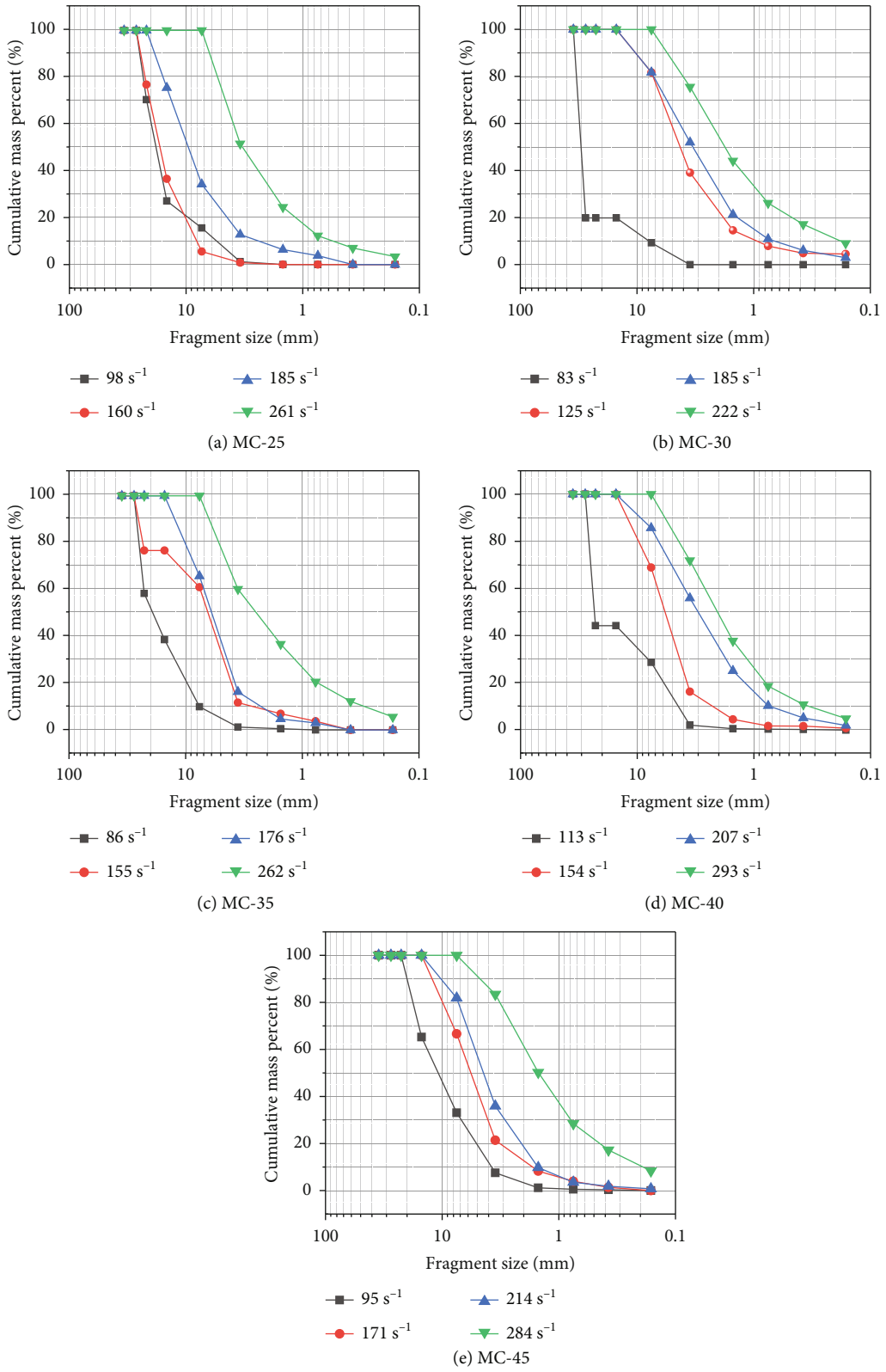

Figure 10: Particle size distribution of mortar-encased specimens.

characteristics of the different mortar-encased specimens in Figures 9(c)–9(g), it can be concluded that the increase in strain rate causes the damage to the five composite samples to be more severe, and the specimens show an obvious progressive failure behavior. The specific performance is as follows: under the condition of low strain rate loading

(~98 s^{-1}), only an axial tensile crack was generated in the external mortar (see Figure 9(c)), but the mortar body was not completely destroyed. When the strain rate was slightly increased (~160 s^{-1}), the mortar body underwent evident axial fracturing, but the inner coal body remained intact and had a bearing capacity. However, as the strain rate continued to increase (~293 s^{-1}), both the external mortar and inner coal pillar exhibited obvious axial fractures, and the shape of the specimen fragments changed from blocks to powder. Therefore, it can be concluded that the external mortar body in the mortar-encased coal pillar system failed first, followed by the coal pillar under impact loads. The presence of an external mortar can change the energy absorption properties of a pillar and prevent impact-induced failure, thereby further protecting the coal pillar. This also reveals that the composite bearing structure exhibits an obvious progressive failure behavior under the action of impact loading.

After impact testing, fragments of the specimens were collected and classified using standard sieves. The mass percentages for the different particle diameters were obtained according to Equations (4) and (5), as shown in Figure 10. It can be noted that mortar-encased coal specimens with different radius ratios have the same fragmentation characteristics. That is, at a given fragment size, the cumulative mass percentage of the fragments gradually increases with increasing strain rate. This result further shows that the impact load is a serious threat to the stability of the mortar-encased coal pillar system when it is sufficiently large.

4. Discussion

In this study, the mortar-encased coal specimen was composed of two parts: coal and mortar elements. The dynamic strength and failure behavior of the composite specimen under impact loads are closely related to the mechanical properties of these two elements. However, the impact load usually acts on the composite specimen in the form of a stress wave, and the absorption rate of the coal and mortar elements to the stress wave energy directly affects the dynamic strength of the composite specimen. Figure 11 shows the energy absorption ratios of the coal and mortar under different impact loads. It can be concluded that the absorption rate of the mortar with respect to the stress wave energy is significantly greater than that of coal for a given incident energy. As reported in previous impact tests [53, 57, 64], the energy absorbed by a specimen is converted into fracture energy consumed by the growth of new cracks. This means that mortar absorbs more energy than coal and produces more deformation under the same impact conditions. Hence, the larger the proportion of mortar in the mortar-encased specimen, the more stress wave energy the specimen can absorb and the higher the dynamic strength of the mortar-encased coal specimen. This conclusion can be confirmed from Figure 7.

The ultimate failure of the composite specimen under dynamic loads is closely related to the failure strain of the coal and mortar elements. Figure 12 presents the stress-strain curves of a single coal specimen (No. SC-2) and a single mortar specimen (No. SM-2) under approximate strain-rate conditions. It can be observed that the single mortar specimen has an obvious postpeak ductile failure stage under impact loads, whereas the single coal specimen shows obvious brittle fracture characteristics. Moreover, the failure strain of the mortar was significantly greater than that of coal. The different mechanical properties ultimately lead to unbalanced deformation of the mortar-encased coal specimen during the postpeak fracture stage. This unbalanced deformation characteristic can also be used to explain why the internal coal body is intact but the external mortar body is damaged under impact loads.

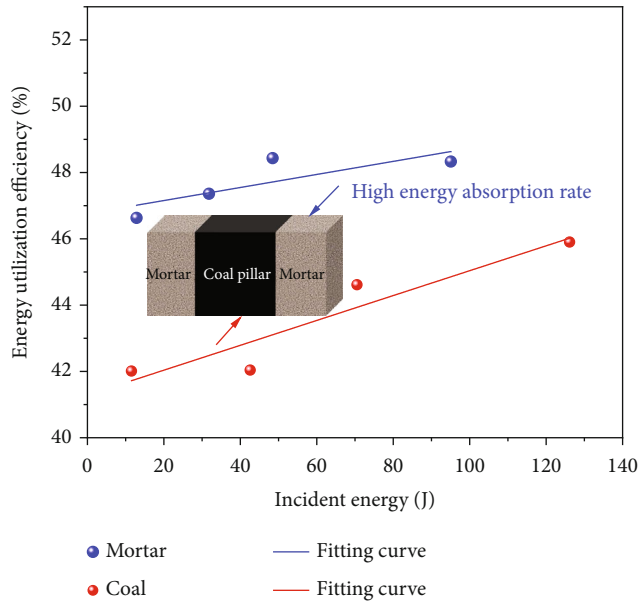

Figure 11: Comparison of the energy utilization ratios of coal and mortar.

The stress-strain curve, progressive failure pattern, and energy dissipation law of the mortar-encased coal specimen under impact loads reflect the instability response of the mortar-encased pillar system. Therefore, the experimental results can also provide useful implications for reinforcing residual coal pillars during underground engineering.

(i) After the coal pillar was wrapped with mortar, a composite bearing structure was formed. External reinforcement is suitable for selecting materials with a higher energy absorption rate of the stress wave, so that the external reinforcement can absorb a large number of stress waves, which increases the energy absorption and shock resistance

(ii) The results show that the greater the thickness of the external mortar, the higher is the dynamic strength of the composite body, which means that the ability of the composite bearing structure to resist impact loads is stronger. Therefore, the encasing thickness should be high if the situation allows

(iii) The failure mode of the mortar-encased specimen induced by impact loads was mainly axial splitting

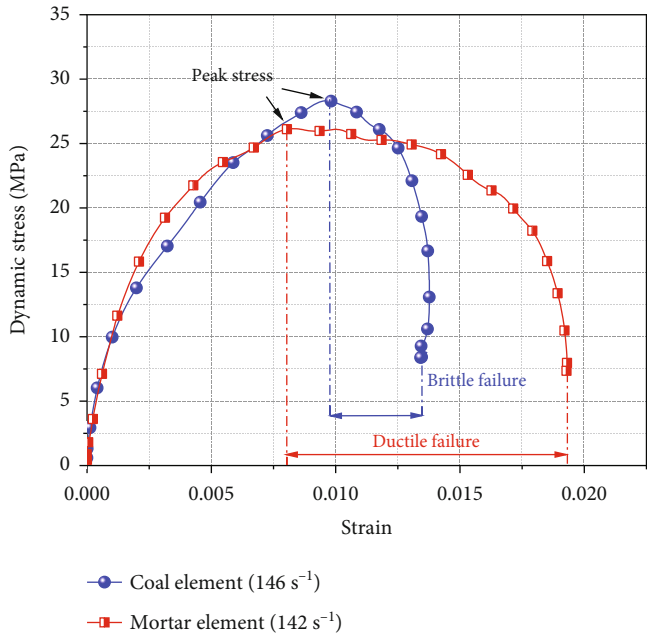

Figure 12: Deformation characteristics of coal and mortar under an approximate strain rate.

failure. A damaged block can easily fall or be thrown into a roadway, causing equipment damage and casualties. Therefore, a layer of anchor nets outside the mortar can be used to reduce the ejection of damaged blocks and ensure the safety of personnel and equipment

5. Conclusions

In this paper, a series of impact tests were conducted on coal, mortar, and mortar-encased coal specimens using a split Hopkinson pressure bar (SHPB) system. The mechanical properties and failure behavior of mortar-encased coal bodies under impact loads were studied. The main results of this work are summarized as follows.

(1) Mortar, coal, and mortar-encased specimens exhibited three stages of elastic deformation, inelastic deformation, and postpeak fracture under impact loading. However, the mortar specimens exhibited obvious ductile failure behavior after the peak point, whereas the coal specimens showed obvious brittle fracture characteristics. Owing to the difference between mortar and coal in terms of mechanical properties, the mortar-encased coal specimen underwent an obvious unbalanced deformation under impact loads

(2) The dynamic strengths of the coal, mortar, and mortar-encased specimens increased with increasing strain rate. Meanwhile, the dynamic strength of the mortar-encased coal specimen increased with the increasing radius of the outer mortar body. Under low-impact loading conditions, the mortar body outside the composite body first experiences axial splitting failure, and the internal coal body remains intact. With increasing strain rate, both the external mortar body and internal coal pillar were damaged, and the failure mode gradually changed from block to powder formation

(3) The energy density and energy absorption rate of the coal, mortar, and mortar-encased specimens all increased linearly with increasing incident energy. For a given incident energy, the energy absorption rate of the mortar is the highest, followed by that of the mortar-encased specimen, and that of the coal is the lowest, which shows that mortar has a better energy absorption effect than coal. In addition, the energy absorption rate of the mortar-encased specimens showed an increasing trend with the increasing thickness of the external mortar

(4) When reinforcing residual coal pillars, the mechanical properties of the external reinforcement should be fully considered. The external reinforcement is a suitable material with a higher stress wave energy absorption rate, so that it can absorb a large number of stress waves, which increases energy absorption and shock resistance. Moreover, the external solid should be as thick as possible, which can improve the anti-interference ability of the composite supporting structure and reduce internal coal pillar damage

Data Availability

The experimental data used to support the findings of this study are included within the article.

Conflicts of Interest

The authors declare no conflict of interest.

Acknowledgments

This work was supported by the National Natural Science Foundation of China (No. 52174125, No. 51925402, and No. 52004171), Outstanding Youth Cultivation Project in Shanxi Province (No. 202103021222008), Shanxi Science and Technology Major Project (No. 20201102004), Opening Fund of Key Laboratory of Mining Disaster Prevention and Control (MDPC202004), and Key Science and Technology Innovation Team of "1331" Project in Shanxi Province.

References

[1] J. A. Wang, X. C. Shang, and H. T. Ma, "Investigation of catastrophic ground collapse in Xingtai gypsum mines in China," *International Journal of Rock Mechanics and Mining Sciences*, vol. 45, no. 8, pp. 1480–1499, 2008.

[2] H. Ma, J. Wang, and Y. Wang, "Study on mechanics and domino effect of large-scale goaf cave-in," *Safety Science*, vol. 50, no. 4, pp. 689–694, 2012.

[3] J. W. Bai, G. R. Feng, Z. H. Wang, S. Y. Wang, T. Y. Qi, and P. F. Wang, "Experimental investigations on the progressive failure characteristics of a sandwiched coal-rock system under uniaxial compression," *Applied Sciences*, vol. 9, no. 6, p. 1195, 2019.

[4] J. X. Yang, C. Y. Liu, B. Yu, and F. F. Wu, "The effect of a multi-gob, pier-type roof structure on coal pillar load-bearing capacity and stress distribution," *Bulletin of Engineering Geology and the Environment*, vol. 74, no. 4, pp. 1267–1273, 2015.

[5] W. B. Zhu, J. L. Xu, and Y. C. Li, "Mechanism of the dynamic pressure caused by the instability of upper chamber coal pillars in Shendong coalfield, China," *Geosciences Journal*, vol. 21, no. 5, article 25, pp. 729–741, 2017.

[6] X. M. Cui, Y. G. Gao, and D. B. Yuan, "Sudden surface collapse disasters caused by shallow partial mining in Datong coalfield, China," *Natural Hazards*, vol. 74, no. 2, pp. 911–929, 2014.

[7] G. R. Feng, J. W. Bai, X. D. Shi et al., "Key pillar theory in the chain failure of residual coal pillars and its application prospect," *Journal of China Coal Society*, vol. 46, no. 1, pp. 164–179, 2020.

[8] X. Q. Zhang, P. L. Gong, K. Wang, J. Z. Li, and Y. L. Jiang, "Characteristic and mechanism of roof fracture ahead of the face in an LTCC panel when passing an abandoned roadway: a case study from the Shenghua Coal Mine, China," *Rock Mechanics and Rock Engineering*, vol. 52, no. 8, pp. 2775–2788, 2019.

[9] L. Y. Tong, L. Leo, B. Amatya, and S. Y. Liu, "Risk assessment and remediation strategies for highway construction in abandoned coal mine region: lessons learned from Xuzhou, China," *Bulletin of Engineering Geology and the Environment*, vol. 75, no. 3, article 760, pp. 1045–1066, 2016.

[10] D. F. Zhu, S. H. Tu, F. T. Wang, and X. S. Ma, "Stability evaluation on pillar system of room and pillar mining in goaf at shallow depth seam," *Journal of China Coal Society*, vol. 43, no. 2, pp. 390–397, 2018.

[11] D. Ma, X. X. Miao, H. B. Bai et al., "Effect of mining on shear sidewall groundwater inrush hazard caused by seepage instability of the penetrated karst collapse pillar," *Natural Hazards*, vol. 82, no. 1, pp. 73–93, 2016.

[12] J. J. Feng, E. Y. Wang, Q. S. Huang, H. C. Ding, and X. Y. Zhang, "Experimental and numerical study of failure behavior and mechanism of coal under dynamic compressive loads," *International Journal of Mining Science and Technology*, vol. 30, no. 5, pp. 613–621, 2020.

[13] L. G. Wang and X. X. Miao, "Study on catastrophe characteristics of the destabilization of coal pillars," *Journal of China University of Mining and Technology*, vol. 36, pp. 7–11, 2009.

[14] R. Frith and G. Reed, "Coal pillar design when considered a reinforcement problem rather than a suspension problem," *International Journal of Mining Science and Technology*, vol. 28, no. 1, pp. 11–19, 2018.

[15] B. A. Poulsen and B. Shen, "Subsidence risk assessment of decommissioned bord-and-pillar collieries," *International Journal of Rock Mechanics and Mining Sciences*, vol. 60, pp. 312–320, 2013.

[16] J. W. Bai, B. Q. Cui, T. Y. Qi et al., "Fundamental theory for rock strata control of key pillar-side backfilling," *Journal of China Coal Society*, vol. 46, no. 2, pp. 424–438, 2021.

[17] C. W. Zhang, Z. X. Jin, G. R. Feng, X. M. Song, R. Gao, and Y. J. Zhang, "Double peaked stress-strain behavior and progressive failure mechanism of encased coal pillars under uniaxial compression," *Rock Mechanics and Rock Engineering*, vol. 53, no. 7, pp. 3253–3266, 2020.

[18] N. Zhou, M. Li, J. X. Zhang, and R. Gao, "Roadway backfill method to prevent geohazards induced by room and pillar mining: a case study in Changxing coal mine, China," *Natural Hazards and Earth System Sciences*, vol. 16, no. 12, pp. 2473–2484, 2016.

[19] Z. T. Bieniawski, "In situ strength and deformation characteristics of coal," *Engineering Geology*, vol. 2, no. 5, pp. 325–340, 1968.

[20] Z. T. Bieniawski, "The effect of specimen size on compressive strength of coal," *International Journal of Rock Mechanics and Mining Science and Geomechanics Abstracts*, vol. 5, no. 4, pp. 325–335, 1968.

[21] T. Hauquin, O. Deck, and Y. Gunzberger, "Average vertical stress on irregular elastic pillars estimated by a function of the relative extraction ratio," *International Journal of Rock Mechanics and Mining Sciences*, vol. 83, pp. 122–134, 2016.

[22] D. Jasinge, P. G. Ranjith, S. K. Choi, J. Kodikara, M. Arthur, and H. Li, "Mechanical properties of reconstituted Australian black coal," *Journal of Geotechnical and Geoenvironmental Engineering*, vol. 135, no. 7, pp. 980–985, 2009.

[23] T. Malli, M. Yetkin, M. Özfirat, and B. Kahraman, "Numerical analysis of underground space and pillar design in metalliferous mine," *Journal of African Earth Sciences*, vol. 134, pp. 365–372, 2017.

[24] S. Y. Wang, S. W. Sloan, M. L. Huang, and C. A. Tang, "Numerical study of failure mechanism of serial and parallel rock pillars," *Rock Mechanics and Rock Engineering*, vol. 44, no. 2, article 116, pp. 179–198, 2011.

[25] D. J. Xue, J. Zhou, Y. T. Liu, and L. Gao, "On the excavation-induced stress drop in damaged coal considering a coupled yield and failure criterion," *International Journal of Coal Science and Technology*, vol. 7, no. 1, pp. 58–67, 2020.

[26] S. Dehghan, K. Shahriar, P. Maarefvand, and K. Goshtasbi, "3-D numerical modelling of Domino failure of hard rock

pillars in Fetr6 Chromite Mine, Iran, and comparison with empirical methods," *Journal of Central South University*, vol. 20, no. 2, article 1517, pp. 541–549, 2013.

[27] C. Mark and Z. Agioutantis, "Analysis of coal pillar stability (ACPS): a new generation of pillar design software," *International Journal of Mining Science and Technology*, vol. 29, no. 1, pp. 87–91, 2019.

[28] B. A. Poulsen and D. P. Adhikary, "A numerical study of the scale effect in coal strength," *International Journal of Rock Mechanics and Mining Sciences*, vol. 63, pp. 62–71, 2013.

[29] E. J. Cording, Y. M. A. Hashash, and J. Oh, "Analysis of pillar stability of mined gas storage caverns in shale formations," *Engineering Geology*, vol. 184, pp. 71–80, 2015.

[30] L. Wang, Y. P. Cheng, C. Xu, F. H. An, K. Jin, and X. L. Zhang, "The controlling effect of thick-hard igneous rock on pressure relief gas drainage and dynamic disasters in outburst coal seams," *Natural Hazards*, vol. 66, no. 2, article 547, pp. 1221–1241, 2013.

[31] W. B. Zhu, L. Chen, Z. L. Zhou, B. T. Shen, and Y. Xu, "Failure propagation of pillars and roof in a room and pillar mine induced by longwall mining in the lower seam," *Rock Mechanics and Rock Engineering*, vol. 52, no. 4, pp. 1193–1209, 2019.

[32] Q. L. Yao, T. Chen, M. H. Ju, S. Liang, Y. P. Liu, and X. H. Li, "Effects of water intrusion on mechanical properties of and crack propagation in coal," *Rock Mechanics and Rock Engineering*, vol. 49, no. 12, pp. 4699–4709, 2016.

[33] F. Gao and H. Kang, "Experimental study on the residual strength of coal under low confinement," *Rock Mechanics and Rock Engineering*, vol. 50, no. 2, pp. 285–296, 2017.

[34] R. D. Peng, Y. Ju, J. G. Wang, H. P. Xie, F. Gao, and L. T. Mao, "Energy dissipation and release during coal failure under conventional triaxial compression," *Rock Mechanics and Rock Engineering*, vol. 48, no. 2, pp. 509–526, 2015.

[35] Z. L. Zhou, L. Chen, X. Cai, B. T. Shen, J. Zhou, and K. Du, "Experimental investigation of the progressive failure of multiple pillar-roof system," *Rock Mechanics and Rock Engineering*, vol. 51, no. 5, pp. 1629–1636, 2018.

[36] M. Z. Gao, J. Xie, J. Guo, Y. Q. Lu, Z. Q. He, and C. Li, "Fractal evolution and connectivity characteristics of mining-induced crack networks in coal masses at different depths," *Geomechanics and Geophysics for Geo-Energy and Geo-Resources*, vol. 7, no. 1, p. 9, 2021.

[37] S. F. Wang, X. B. Li, and S. Y. Wang, "Separation and fracturing in overlying strata disturbed by longwall mining in a mineral deposit seam," *Engineering Geology*, vol. 226, pp. 257–266, 2017.

[38] B. Chen, "Stress-induced trend: the clustering feature of coal mine disasters and earthquakes in China," *International Journal of Coal Science and Technology*, vol. 7, no. 4, pp. 676–692, 2020.

[39] B. Xiao, S. G. Liu, Z. W. Li et al., "Geochemical characteristics of marine shale in the Wufeng Formation-Longmaxi Formation in the northern Sichuan Basin, South China and its implications for depositional controls on organic matter," *Journal of Petroleum Science and Engineering*, vol. 203, article 108618, 2021.

[40] G. R. Feng, Y. J. Zhang, T. Y. Qi, and L. X. Kang, "Status and research progress for residual coal mining in China," *Journal of China Coal Society*, vol. 45, no. 1, pp. 151–159, 2020.

[41] S. F. Wang, X. B. Li, J. R. Yao et al., "Experimental investigation of rock breakage by a conical pick and its application to non-explosive mechanized mining in deep hard rock," *International Journal of Rock Mechanics and Mining Sciences*, vol. 122, article 104063, 2019.

[42] C. J. Fan, H. O. Wen, S. Li, G. Bai, and L. J. Zhou, "Coal seam gas extraction by integrated drillings and punchings from the floor roadway considering hydraulic-mechanical coupling effect," *Geofluids*, vol. 2022, Article ID 5198227, 2022.

[43] C. J. Fan, S. Li, D. Elsworth, J. Han, and Z. H. Yang, "Experimental investigation on dynamic strength and energy dissipation characteristics of gas outburst-prone coal," *Energy Science and Engineering*, vol. 8, no. 4, pp. 1015–1028, 2020.

[44] D. Y. Li, Z. Y. Han, X. L. Sun, T. Zhou, and X. B. Li, "Dynamic mechanical properties and fracturing behavior of marble specimens containing single and double flaws in SHPB tests," *Rock Mechanics and Rock Engineering*, vol. 52, no. 6, article 1652, pp. 1623–1643, 2019.

[45] Y. X. Zhou, K. Xia, X. B. Li et al., "Suggested methods for determining the dynamic strength parameters and mode-I fracture toughness of rock materials," *International Journal of Rock Mechanics and Mining Sciences*, vol. 49, pp. 105–112, 2012.

[46] ISRM, International Society for Rock Mechanics, "Suggested methods for determining tensile strength of rock materials," *International Journal of Rock Mechanics and Mining Science and Geomechanics Abstracts*, vol. 15, no. 3, pp. 99–103, 1978.

[47] W. Wang, H. M. Li, R. F. Yuan, H. L. Gu, C. Wang, and H. G. Li, "Micromechanics analysis and mechanical characteristics of water-saturated coal samples under coupled static-dynamic loads," *Journal of China Coal Society*, vol. 41, pp. 611–617, 2016.

[48] X. B. Li, Z. L. Zhou, T. Lok, L. Hong, and T. B. Yin, "Innovative testing technique of rock subjected to coupled static and dynamic loads," *International Journal of Rock Mechanics and Mining Sciences*, vol. 45, no. 5, pp. 739–748, 2008.

[49] H. Kolsky, "An investigation of the mechanical properties of materials at very high rates of loading," *Proceedings of the Physical Society Section B*, vol. 62, no. 11, pp. 676–700, 1949.

[50] E. D. H. Davies and S. C. Hunter, "The dynamic compression testing of solids by the method of the split Hopkinson pressure bar," *Journal of the Mechanics and Physics of Solids*, vol. 11, no. 3, pp. 155–179, 1963.

[51] D. J. Frew, M. J. Forrestal, and W. Chen, "A split Hopkinson pressure bar technique to determine compressive stress-strain data for rock materials," *Experimental Mechanics*, vol. 41, no. 1, pp. 40–46, 2001.

[52] R. Chen, K. Xia, F. Dai, F. Lu, and S. N. Luo, "Determination of dynamic fracture parameters using a semi-circular bend technique in split Hopkinson pressure bar testing," *Engineering Fracture Mechanics*, vol. 76, no. 9, pp. 1268–1276, 2009.

[53] B. Song and W. Chen, "Energy for specimen deformation in a split Hopkinson pressure bar experiment," *Experimental Mechanics*, vol. 46, no. 3, pp. 407–410, 2006.

[54] Q. B. Zhang and J. Zhao, "A review of dynamic experimental techniques and mechanical behaviour of rock materials," *Rock Mechanics and Rock Engineering*, vol. 47, no. 4, article 463, pp. 1411–1478, 2014.

[55] Z. L. Yan, F. Dai, Y. Liu, and H. B. Du, "Experimental investigations of the dynamic mechanical properties and fracturing behavior of cracked rocks under dynamic loading," *Bulletin of Engineering Geology and the Environment*, vol. 79, no. 10, pp. 5535–5552, 2020.

[56] Z. X. Zhang, S. Q. Kou, L. G. Jiang, and P. A. Lindqvist, "Effects of loading rate on rock fracture: fracture characteristics and energy partitioning," *International Journal of Rock Mechanics and Mining Sciences*, vol. 37, no. 5, pp. 745–762, 2000.

[57] C. J. Li, Y. Xu, P. Y. Chen, H. L. Li, and P. J. Lou, "Dynamic mechanical properties and fragment fractal characteristics of fractured coal–rock-like combined bodies in split Hopkinson pressure bar tests," *Nature Resource Research*, vol. 29, no. 5, pp. 3179–3195, 2020.

[58] L. Weng, Z. J. Wu, Q. Liu, and Z. Wang, "Energy dissipation and dynamic fragmentation of dry and water-saturated siltstones under sub-zero temperatures," *Engineering Fracture Mechanics*, vol. 220, article 106659, 2019.

[59] X. Cai, Z. L. Zhou, and X. M. Du, "Water-induced variations in dynamic behavior and failure characteristics of sandstone subjected to simulated geo-stress," *International Journal of Rock Mechanics and Mining Sciences*, vol. 130, article 104339, 2020.

[60] F. Dai, S. Huang, K. Xia, and Z. Tan, "Some fundamental issues in dynamic compression and tension tests of rocks using split Hopkinson pressure bar," *Rock Mechanics and Rock Engineering*, vol. 43, no. 6, pp. 657–666, 2010.

[61] N. N. Li, Y. Q. Zhou, and H. B. Li, "Experimental study for the effect of joint surface characteristics on stress wave propagation," *Geomechanics and Geophysics for Geo-Energy and Geo-Resources*, vol. 7, no. 3, p. 50, 2021.

[62] J. B. Zhu, W. Y. Bao, Q. Peng, and X. F. Deng, "Influence of substrate properties and interfacial roughness on static and dynamic tensile behaviour of rock-shotcrete interface from macro and micro views," *International Journal of Rock Mechanics and Mining Sciences*, vol. 132, article 104350, 2020.

[63] Z. Q. Yin, W. S. Chen, H. Hao et al., "Dynamic compressive test of gas-containing coal using a modified split Hopkinson pressure bar system," *Rock Mechanics and Rock Engineering*, vol. 53, no. 2, article 1955, pp. 815–829, 2020.

[64] H. Schuler, C. Mayrhofer, and K. Thoma, "Spall experiments for the measurement of the tensile strength and fracture energy of concrete at high strain rates," *International Journal of Impact Engineering*, vol. 32, no. 10, pp. 1635–1650, 2006.